J Mater Sci (2022) 57:563–575

Energy materials

Mixed-valence manganese oxide/reduced graphene oxide composites with enhanced pseudocapacitive performance

Di Guo[1,*], Zhirui Hu[1], Qian Li[1], Lijun Bian[1], Yu Song[1], and Xiaoxia Liu[1,*]

[1] *Department of Chemistry, Northeastern University, Shenyang 110819, People's Republic of China*

Received: 23 July 2021
Accepted: 9 October 2021
Published online: 3 January 2022

© The Author(s), under exclusive licence to Springer Science+Business Media, LLC, part of Springer Nature 2021

ABSTRACT

As typical pseudocapacitive materials, manganese oxides have attracted great interest due to their high theoretical specific capacitance, abundant oxidation states and crystal structures. However, it is still struggling from inferior electrical conductivity, which comes from their natural properties and limited structure used. In this paper, we fabricate hierarchical mixed-valence manganese oxide/graphene on flexible carbon cloths via a hydrothermal method combined with annealing treatment strategy for improving capacitive performance. The microstructure and electrochemical performance of manganese oxide/reduced graphene oxide (MnO_x/G) electrodes obtained at different annealing temperature (400–700 °C) are investigated. Evidenced by XRD, XPS and TEM, MnO_x/G composites consisted of α-MnO_2, hexagonal Mn_2O_3 and cubic MnO are achieved as the annealing temperature increased. The results reveal that the phase of MnO_x, valence state of Mn as well as the pseudocapacitance can be regulated by varying the annealing temperature, and the mixed-valence state in the MnO_x/G-400 composite boost pseudocapacitive property significantly. The MnO_x/G-400 electrode yields the highest areal capacitance of 2.29 F cm^{-2} (437 F g^{-1}) and remarkable stability compared to other MnO_x-based electrodes, which is attributed to the favored electron transfer between Mn species ($Mn^{4+} \leftrightarrow Mn^{3+}$), decreased charge transfer resistance and more active sites between different phase interfaces.

Handling Editor: Joshua Tong.

Address correspondence to E-mail: guodi@mail.neu.edu.cn; xxliu@mail.neu.edu.cn

https://doi.org/10.1007/s10853-021-06613-7

GRAPHICAL ABSTRACT

This work reports the synthesis of hierarchical mixed-valence manganese oxide/reduced graphene oxide composites on flexible carbon cloths via a hydrothermal method combined with annealing treatment strategy for improving capacitive performance.

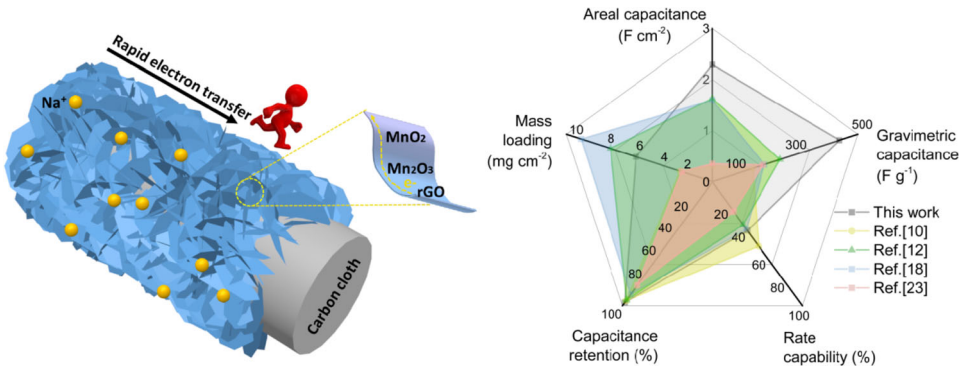

Introduction

Supercapacitors, as typical electrochemical energy storage devices, have been applied ranging from portable electronics to hybrid electrical vehicles owing to their high power densities and long lifetime [1–3]. However, traditional double-layer capacitors based on carbon-based materials can only store low energy, which limited their practical applications in high energy systems. Recently, researchers are focusing on the pseudocapacitive materials with higher specific capacitance and energy density, because the charge stored through not only ion adsorption but also near surface redox reactions. Pseudocapacitive materials mainly include transition metal oxides and conductive polymer. Among various candidates, manganese oxides show significant advantages such as the abundant resources, environmentally friendly nature and high theoretical capacitance (1370 F g^{-1}) [4–8]. More importantly, MnO_2 is usually applied in neutral aqueous electrolytes with a wide potential window, resulting in higher energy density than that of other cathode materials such as NiO, Co_3O_4, PANI.

Nevertheless, the electron conductivity of MnO_2 is poor due to its wide forbidden band. Thus, to obtain satisfying capacitive performance, it is a versatile method of confining or embedding MnO_2 into the carbonaceous materials to form hierarchical composites, which can improve the electrical conductivity and accommodate the large volume changes. Graphene can be a potential choice for improving the electrical conductivity and electrochemical activity of electrode material. It is known that graphene prepared via chemical methods has many advantages including high specific surface area, good electrical conductivity, surface functional groups and stable mechanical structure. Therefore, electrochemical properties of metal oxides can be improved by introducing graphene sheets to construct hierarchical composites. This can effectively improve the charge transport and ion diffusion in the electrodes, and help to relieve volume expansion during electrochemical cycling. Yet, there is still a severe problem for the MnO_2 electrodes, the active material loading is usually small (less than 1 mg cm^{-2}) or rather thin film structure is generally utilized [9–13]. Although the specific capacitance from low mass loading seems high, in fact, the total capacitance and energy stored in the materials is still small, seriously limiting practical applications [14–25]. Generally, providing available energy for commercial devices requires a typical active material mass loading of

5–10 mg cm^{-2} [26–29]. However, increasing the mass loading would lead to slower ion diffusion, worse electrical conductivity and less stable mechanical structure of the oxide active materials, declining the electrochemical activity. An efficient strategy to improve the capacitive property of large mass loading materials is to fabricate a hierarchical structure and combination with highly conductive materials [30–36]. For example, Hu et al. [34] synthetized a symmetrical MnO_2-carbon nanotube structure with a large mass loading of 8.3 mg cm^{-2}, leading to a high areal capacitance of 2.8 F cm^{-2} at a scan rate of 0.05 mV s^{-1}. The RGO-MnO_2-PPy electrode prepared by Wang et al. exhibited high electrochemical performance at large mass loadings, in addition, the specific capacitance of assembled asymmetric supercapacitor increased with an increase in the mass loading [35]. Zhou's group demonstrated an Al doped α-MnO_2 electrode with a specific capacitance of 213 F g^{-1} possessing a high mass loading of 4 mg cm^{-2}, and it showed satisfying cyclic performance of 91% capacitance rentention maintained after 15,000 cycles [36].

Herein, we demonstrate an investigation on the composite consisted of mixed-valence manganese oxide and rGO with different morphologies and structures. Using a facile hydrothermal technique, we can prepare a series of MnO_x/G electrodes on carbon cloths by controlling the annealing temperature, with a relatively high mass loading of 5–8 mg cm^{-2}. Impressively, as the annealing temperature varies, the crystalline phase of product transforms from α-MnO_2 into Mn_2O_3 and (or) MnO. So far, there have been some reported works about two-phase or multiphase metal oxide composites that have the potential to show better performances for electrochemical energy storage [37–44]. In this work, α-MnO_2/ Mn_2O_3 composite annealed at 400 °C exhibits increased capacitance, improved rate capability and outstanding cyclic stability, benefiting from enhanced electrochemical activity. The result indicates the full utilization of active materials, fast reaction kinetics and mechanical stability of composite materials during charge/discharge process. Besides, the rGO not only contributes to the total capacitance but also improves the electrical conductivity of the whole electrode.

Experimental details

Materials

All used chemicals in our work were purchased from Sinopharm Chemical Reagent Co., Ltd. and without further purification. Carbon cloth was purchased from Fuel Cell Earth (United States), and graphene oxide powders manufactured via traditional Hummer's method were from Institute of coal chemistry, Chinese academy of science.

Synthesis of mixed-valence MnO_x/G composites

Before the preparation, a piece of carbon cloth substrate (2 × 3 cm^2) was rinsed with water and ethanol for 30 min, respectively. Firstly, under constant magnetic stirring, 5 mmol of $KMnO_4$ was added to 20 ml of distilled water to form homogeneous solution and moved to a Teflon-lined stainless steel autoclave liner. The treated carbon cloth substrate was put into the liner, immersed into the reaction solution and maintained at 150 °C for 6 h. After the reaction was over, the carbon cloth wrapped with MnO_2 sample was taken out and washed by amount of deionized water, in order to remove the residual nanoparticle debris or extra ions, then dried at 60 °C under vacuum overnight. Secondly, the obtained MnO_2 sample was immersed into a 20 ml of suspension included 50 mg of GO powders and MnO_2/G composites were achieved through a secondary hydrothermal reaction at 90 °C for 2 h. Finally, to investigate the influence of annealing temperature on MnO_x/G, the MnO_2/G sample was annealed at 400 °C, 500 °C, 600 °C and 700 °C for 1 h in pure N_2. The as-prepared samples were denoted as MnO_x/G-400, MnO_x/G-500, MnO_x/G-600 and MnO_x/G-700 sample, respectively. All the samples were weighed and the active material loading of MnO_2, MnO_2/G, MnO_x/G-400, MnO_x/G-500, MnO_x/G-600 and MnO_x/G-700 was 6.19, 5.30, 5.24, 5.21, 5.18 and 5.07 mg cm^{-2}, respectively. The mass loading of Mn_xO/G in this work can be controlled by varying the concentration of $KMnO_4$ and the hydrothermal reaction time.

Characterization and electrochemical measurements

Morphologies of the composites were studied by a field emission scanning electron microscope (Ultra Plus, Carl Zeiss, Germany). The crystal structures of the samples were analyzed by X-ray diffraction (X'Pert Pro, PANalytical B.V.). A laser Raman spectrometer (Labram-010, 632 nm) was used to collect Raman spectra. Thermogravimetric (TG) measurements were performed on a Netzsch STA 449 F3 Jupiter analyzer. X-ray photoelectron spectroscopy (XPS) was collected using an XPS spectrometer (ESCALAB 250Xi, USA). The mass loading of active materials was measured using a Sartorius BT 25 S semi-microbalance with a sensitivity of 0.01 mg. Capacitive properties of manganese oxide-based electrodes were investigated in three-electrode cells included a SCE as the reference and graphite foil as the counter electrodes, 1 M Na_2SO_4 solution as electrolyte.

Results and discussion

Figure 1a exhibits the procedure to synthesize the MnO_x/G-based hybrid electrodes, which included a two-step hydrothermal route and annealing treatment. Firstly, the MnO_2 nanoclusters are prepared via a typical redox reaction of $KMnO_4$ and carbon cloth substrate. Secondly, the obtained MnO_2 electrode is coated with reduced graphene oxide nanosheets via a second hydrothermal reaction. Thirdly, annealing at various temperatures can transform MnO_2/G to the MnO_x/G composite consisted of different valence states of Mn. In the hydrothermal process, carbon cloths not only act as flexible substrates, but also take part in the reaction as reducing agents, which make the active material of MnO_2/G has strong interactions with current collectors. After calcination, the MnO_2 is reduced into manganese oxides at lower valence states and rGO may work as the reductant. With the calcination temperature increasing, the mass loading of active

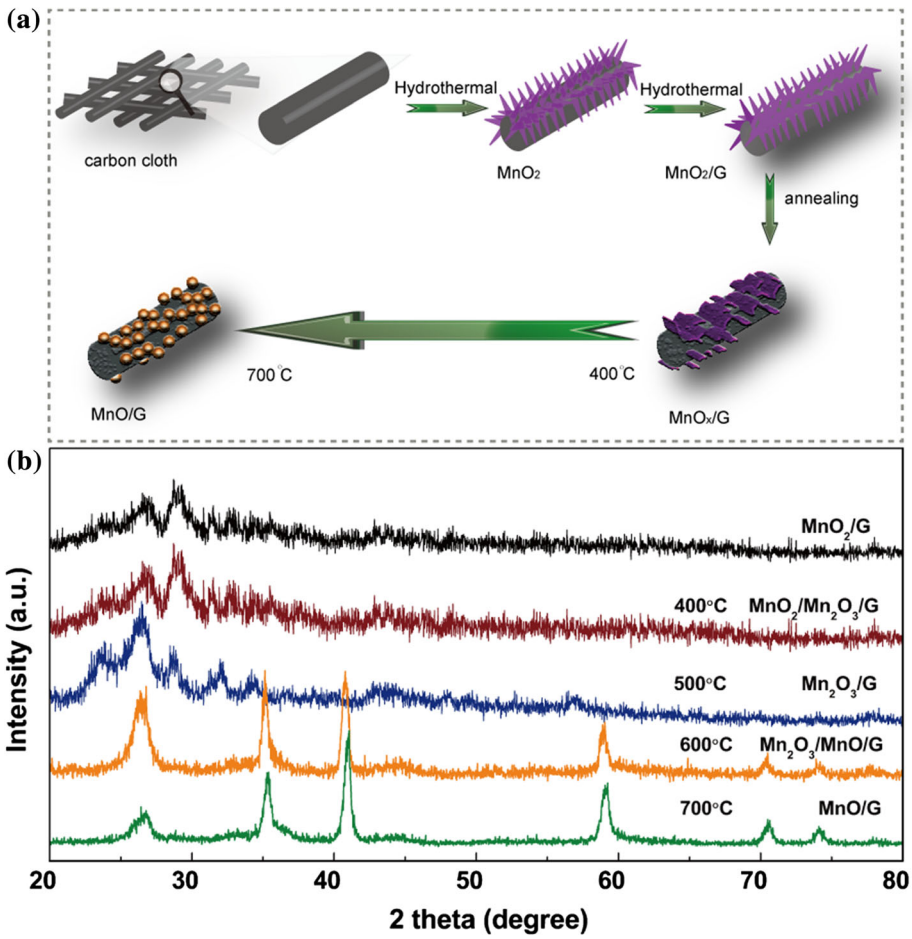

Figure 1 **a** Illustration of the procedure to prepare the MnO_x/G composites. **b** XRD patterns of MnO_2/G and MnO_x/G electrodes after annealing at the temperature of 400 °C, 500 °C, 600 °C, and 700 °C.

materials declined gradually. Finally, the net-like structure consisted of MnO_x nanoplates turned into small nanoparticles of MnO. We conducted XRD measurements for the MnO_2/G and MnO_x/G prepared after annealing. Figure 1b shows the XRD patterns of the composites. To avoid the strong diffraction signals distraction from the carbon cloth substrate, the active materials were scratched from the carbon cloth for XRD analysis. In the MnO_2/G, all the collected diffraction peaks can be indexed to α-MnO_2 (JCPDS no. 24–0735) except a broad peak at 26.8° is relate to the (002) plane of rGO. According to the XRD patterns of the other samples, the diffraction signals are corresponding to hexagonal Mn_2O_3 (JCPDS no. 33–0900) and cubic MnO (JCPDS no. 07–0230) except the peaks of the rGO [9, 16].

The morphologies of MnO_2 and MnO_2/G composites were investigated by SEM. Figure 2a displays the microstructure evolvement of pristine MnO_2. Clearly, As can be seen, each fiber of carbon cloth substrates are covered with MnO_2 nanoclusters tightly and uniformly, forming a hierarchical nanostructure like "core–shell" type with an enlarged specific surface area, beneficial for electrolyte ion insertion and fast electron transfer. According to the high magnification SEM image in Fig. 2c and d, the morphology of MnO_2 electrodes remain essentially unchanged after combination with rGO nanosheets. Figure 3 shows the SEM images of MnO_x/G-based electrodes obtained from different annealing temperatures, disclosing the morphological evolution of MnO_x/G. At 400 °C, many dense and small MnO_x/G nanosheets were distributed at the surface of the carbon cloth substrate uniformly. From 400 to 600 °C, these nanosheets started to become larger and formed a net-like morphology with pore structure (Fig. 3a–f). The MnO_x/G-400, MnO_x/G-500 and MnO_x/G-600 showed the loose and porous nanostructure constructed by the large nanosheets, which formed many pores beneficial for ion diffusion and electron transfer. Upon further increased temperature to 700 °C, the nanosheets disappeared and the surface was covered by agglomerated nanoparticles (Fig. 3g, h).

The pseudocapacitive properties were studied for the MnO_x-based electrodes (MnO_2, MnO_2/G, MnO_x/G-400, MnO_x/G-500, MnO_x/G-600 and MnO_x/G-700) in a three-electrode system containing 1 M Na_2SO_4 electrolyte. Our prepared composite samples are used as the working electrodes, saturated calomel electrode and graphite foil act as the reference and counter electrode, respectively. The cyclic voltammetry (CV) curves of the MnO_x/G electrodes at 5 mV $s^{-1}$are displayed in Fig. 4a. It can be observed

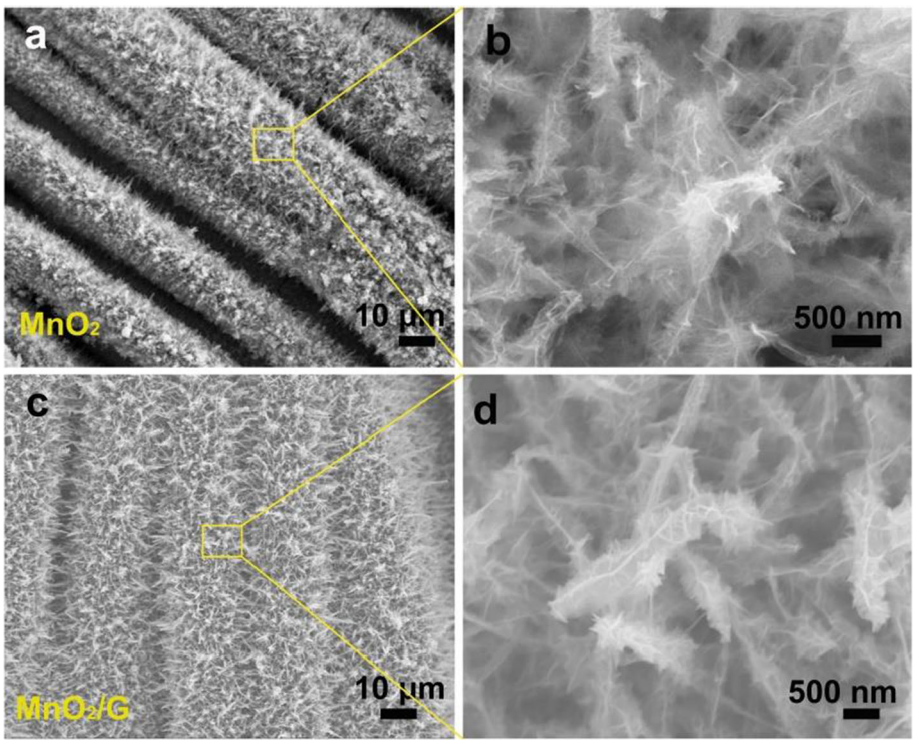

Figure 2 SEM images of the MnO_2 **a**, **b** and MnO_2/G **c**, **d**.

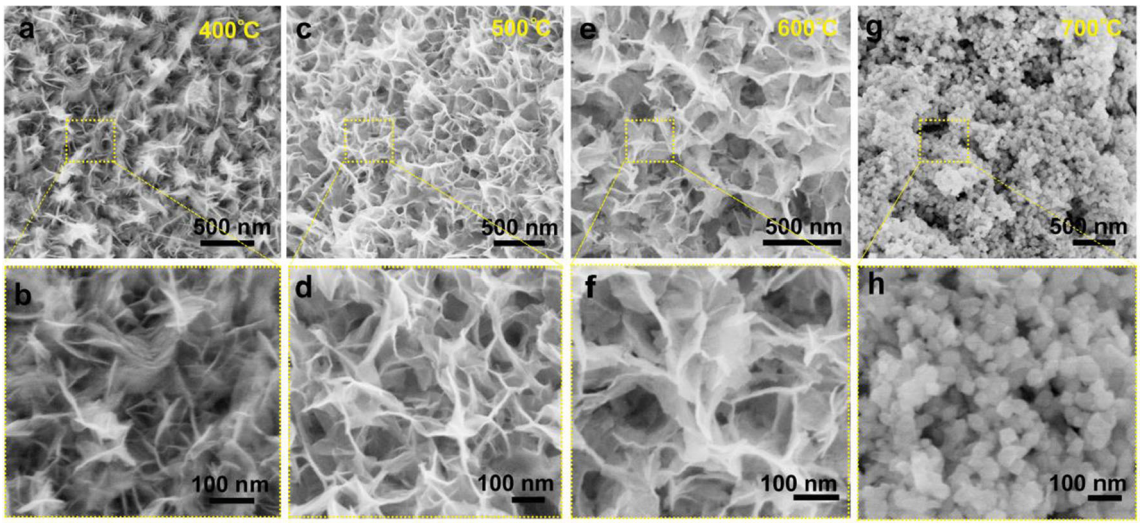

Figure 3 SEM images of MnO_x-400 **a**, **b**, MnO_x-500 **c**, **d**, MnO_x-600 **e**, **f** and MnO_x-700 g, **h**.

that the current density and integral area of CV curve increase significantly after the MnO_2 is coated with rGO, which is attributed to the better electron transfer ability, more active sites and double-layer capacitance provided by the rGO. When the annealing temperature reached to 400 °C, the current density increased dramatically. However, further raising annealing temperature leads to the decreased capacitance, the capacitance of the MnO_x/G-500 ~ MnO_x/G-700 sample were lower than MnO_x/G-400. The galvanostatic charge–discharge (GCD) results exhibit the same trend. In Fig. 4b, the GCD profiles of various electrodes at the current density of 5 mA cm^{-2} are provided. Areal capacitances of different samples according to the constant current charge–discharge profiles are calculated from Eq. 1 [37, 38]:

$$C_A = \frac{It}{\Delta U} \quad (1)$$

where C_A stands for specific capacitance (F cm^{-2}), I is the discharge current density (A cm^{-2}), t is the discharge time (s), ΔU represents the potential window (V). As shown in Fig. 4c, the MnO_x/G-400 sample exhibited the highest capacitance under the same tested conditions. At the current density of 5 mA cm^{-2}, MnO_x/G-400 displayed a higher areal capacitance of 1.52 F cm^{-2} (a gravimetric capacitance of 290 F g^{-1} with a large mass loading of 5.24 mg cm^{-2}) than the other samples (MnO_2, 0.51 F cm^{-2}; MnO_2/G, 0.64 F cm^{-2}; MnO_x/G-500, 1.01 F cm^{-2}; MnO_x-600, 0.90 F cm^{-2}; and MnO_x/G-700, 0.46 F cm^{-2}). Though the MnO_x/G-400 showed the highest capacitance, its rate capability was not satisfied, while the MnO_x/G-500 electrode yielded better rate capability with 64% capacitance retained at the high current density of 20 mA cm^{-2} (0.84 F cm^{-2}). By comparison, when the current density increased from 1 to 20 mA cm^{-2}, the capacitances of other samples fade much faster with the increase of current, with only 16% (0.2 F cm^{-2} for MnO_2), 18% (0.24 F cm^{-2} for MnO_2/G), 40% (0.9 F cm^{-2} for MnO_x/G-400), 58% (0.67 F cm^{-2} for MnO_x/G-600), and 38% (0.27 F cm^{-2} for MnO_x/G-700) areal capacitance remaining (Fig. 4c). These results indicate that morphology and crystal structure play important roles on the charge storage capability of the MnO_x/G materials. The optimized material MnO_x/G-400 with higher capacitance and better rate capability own an open net-like structure that is constructed of MnO_x/G nanosheets. Based on XRD results, the main component of MnO_x/G-400 (MnO_2/Mn_2O_3/G) is mixed manganese oxides consisted of Mn^{4+} and Mn^{3+}, which contributed to the prominent pseudocapacitance. Mn^{3+} replaced part of Mn^{4+} in the MnO_x/G, so the net negative charge is balanced by inserting foreign cations such as Na^+. Generally, the electrical conductivity of single compound is lower than that of mixed compounds due to the existence of oxygen vacancy in the composites [45–47]. The above electrochemical results further confirm that the phase transition can improve the electrical conductivity of pure MnO_x electrodes. To further study the electrochemical performance, the series of MnO_x/G electrodes were investigated by electrochemical

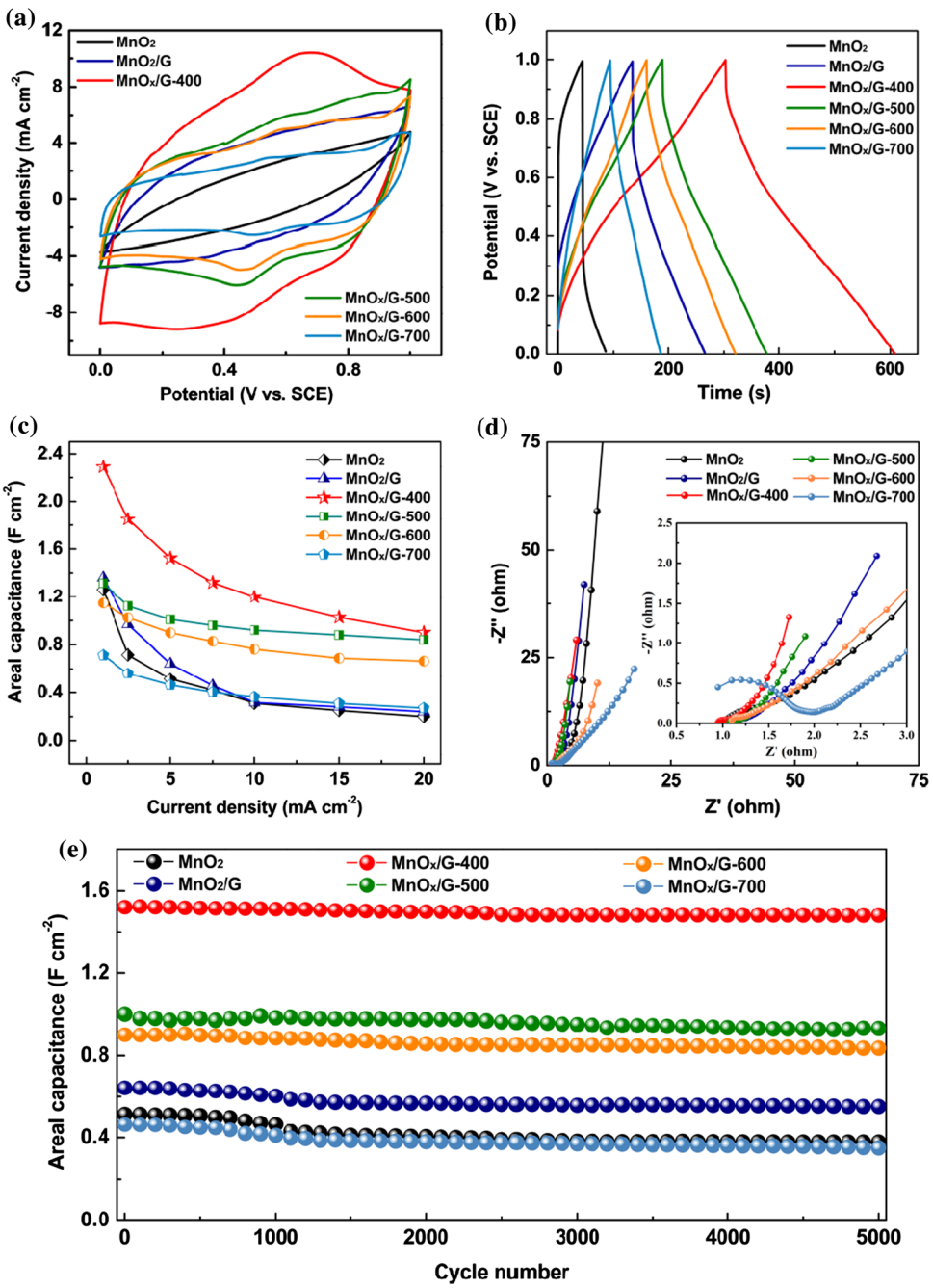

Figure 4 Electrochemistry performance of the six MnO_x-based electrodes: **a** CV curves measured at a scan rate of 5 mV s^{-1}. **b** Charge–discharge profiles measured at 5 mA cm^{-2}. **c** Areal capacitance measured at different current densities in the potential range of 0 − 1.0 V. **d** The Nyquist plots for six MnO_x-based electrodes (inset: the enlarged view of high frequency region). **e** Cycling stability of the six MnO_x-based electrodes.

impedance spectroscopy (EIS). As shown in Fig. 4d, for the MnO_x/G-based electrodes, with the annealing temperature up to 400 °C and 500 °C, the Warburg impendence of both electrodes are lower than that of MnO_2/G before annealing drastically. In the low frequency region, the slope of MnO_x/G-400 is higher than that of other samples, suggesting that MnO_x/G-400 has more rapid ion diffusion rate. As for the high frequency region, the equivalent series resistance (R_s) of the MnO_x/G-400 electrode was only 0.92 Ω, indicating small intrinsic impendence (the inset of Fig. 5d). Compared to other samples, MnO_x/G-400 also exhibited smaller charge transfer resistance (R_{ct}), leading to a faster charge transfer process at the electrode/electrolyte interface and larger charge storage.

The cyclic stability of the MnO_x/G-based electrodes is shown in Fig. 4e. Among all the samples, the areal capacitance of the MnO_x/G-400 electrode was highest and it also showed excellent capacitance

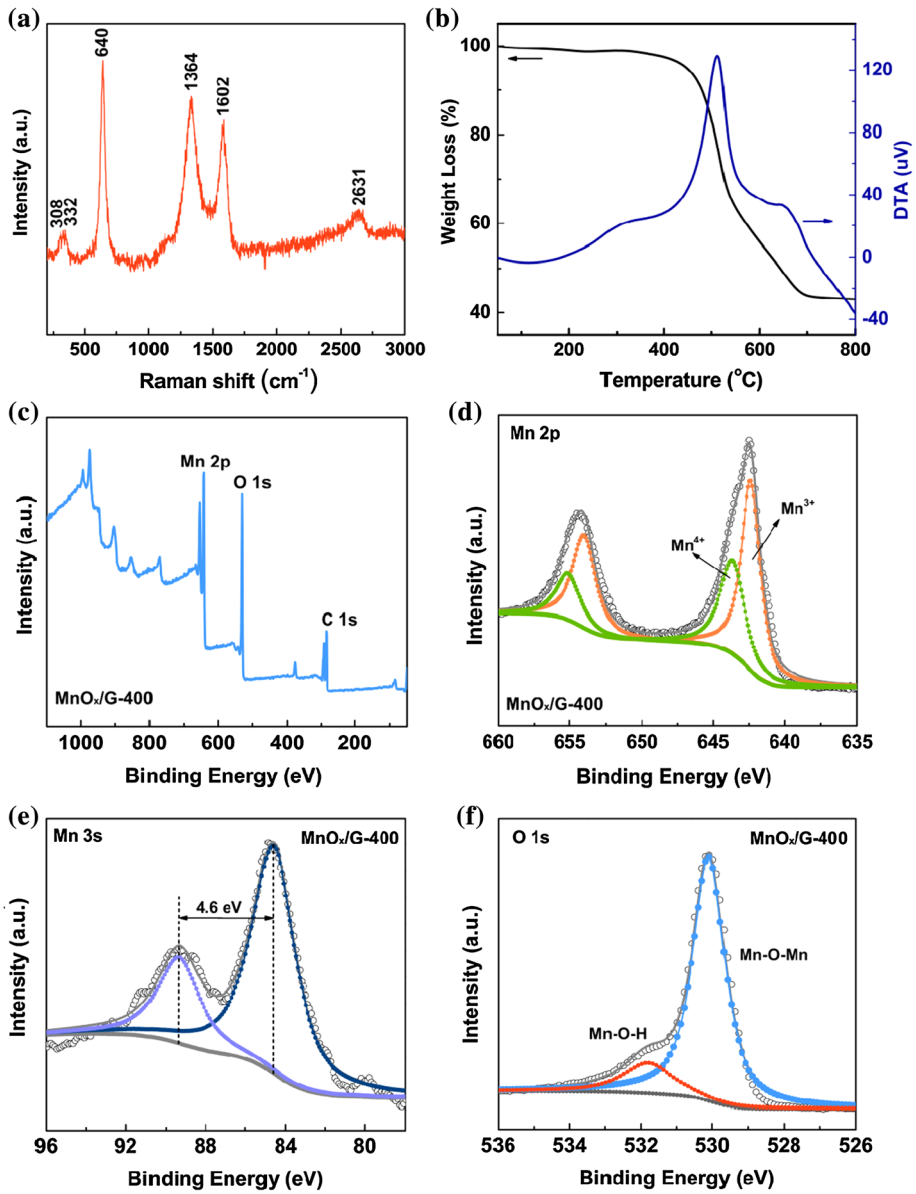

Figure 5 **a** Raman spectrum of MnO_x/G-400. **b** TG curve of MnO_x/G-400. **c** XPS spectrum of MnO_x/G-400. **d** Mn 2p, **e** Mn 3 s and **f** O 1 s XPS spectra of the MnO_x/G-400 electrode.

retention of 97.4% after 5000 charge/discharge cycles at 5 mA cm^{-2}. On the contrary, the MnO_2, MnO_2/G, MnO_x/G-500, MnO_x/G-600 and MnO_x/G-700 electrode showed a decay of capacitance, with 76.3%, 85.8%, 93.2%, 92.7% and 75.4% remaining. During the first 600 cycles, the capacitance of MnO_x/G-500 increased from 1.0 to 1.1 F cm^{-2} because of the gradual diffusion of electrolyte ions into the entire electrode. A high capacitance retention of 93.2% for MnO_x/G-500 can be observed and MnO_x-600 electrode also showed a similar retention of 92.7% capacitance. But, due to the small initial capacitance of the two samples, obtained capacitance after cycling was still small. In the MnO_x/G-500 and MnO_x/G-600 electrodes, the porous morphologies constructed by the large nanosheets can ensure the good flexibility and help to buffer the internal strain created during cycling. The poor cycling stability of MnO_2 and MnO_2/G was mainly attributed to the dissolution of Mn (II) during the charge/discharge process caused by the disproportionation reaction of generated Mn (III) from the Jahn–Teller effect [29, 34, 48–50]. In addition, the long-term cyclic stability of MnO_x/G-400 electrode was also tested, shown in Fig. S1. The 91.4% capacitance of the composite electrode was retained after 10,000 cycles at a current density of 5 mA cm^{-2}, illustrating excellent cyclic stability of the as-prepared MnO_x/G-400 electrode. The

comparison of the recently reported Mn-based electrodes with different components for supercapacitors is displayed in Table S1.

To further explore the structural characteristics and explain best pseudocapacitive performance of MnO_x/G-400, the vibrational properties of the MnO_x/G-400 composite were investigated by Raman spectra (Fig. 5a). The G band at 1602 cm^{-1} and the D band at 1364 cm^{-1} can be seen, evidently come from the rGO sheets. Whereas another sharp band at 640 cm^{-1} is contributed to the symmetric M–O stretching vibration of MnO_6 groups [39, 40]. Moreover, the value of I_D/I_G, that is, the intensity ratio of the D to the G band for rGO can be calculated as 1.1805, indicating level of graphene disorder/defects in the composite. The thermogravimetric analysis (TGA) and differential scanning calorimetry (DSC) results of MnO_x/G-400 are shown in Fig. 5b. The mass percentage of MnO_x is nearly 43%. The X-ray photoelectron spectroscopy (XPS) was also investigated to reveal the chemical compositions and Mn valence states. Figure 5c shows the complete XPS spectrum of the MnO_x/G-400 including the signal of the Mn, O and C element. The XPS peaks of Mn 2p orbit in Fig. 5d were fitted to confirm the presence of Mn^{3+} and Mn^{4+}. The peaks at 642.4 eV and 643.7 eV corresponded to the Mn^{3+} and Mn^{4+} peaks of $2p_{3/2}$ orbit, respectively [41, 51–53]. The atomic ratio of Mn^{3+}/Mn^{4+} was calculated to 1.6:1 according to the area of fitting peaks, indicating the quality percentage of MnO_2 and Mn_2O_3 are 40.8% and 59.2%, respectively. The energy separations (ΔE) of Mn 3 s peaks were measured to be 4.6 eV for the MnO_x/G-400 sample, confirming the reduced Mn oxidation state with increased annealing temperature (Fig. 5e). Based on the linear relationship between ΔE value and valence state of Mn, the average oxidation state of Mn in the MnO_x/G-400 sample was calculated to be 3.4, which was in accordance with the Mn $2p_{3/2}$ XPS spectra and XRD spectrum. Figure 5f shows the fitting peaks of O 1 s orbit of MnO_x/G-400. The peaks located at 530.1 eV and 531.8 eV are attributed to Mn–O-Mn and Mn–O-H, which mainly come from the MnO_x in the composite [42]. In contrast, the XPS spectrum of the MnO_2/G was also tested and displayed in Fig. S2 in the Supporting Information. Fig. S2(a) shows the complete XPS spectrum of the MnO_2/G with the signal of the Mn, O and C element. The XPS peaks of Mn 2p orbit located at 642.3 eV and 654.1 eV corresponded to Mn^{4+} (Fig.S2(b)). The ΔE (4.2 eV) of Mn 3 s peaks for the MnO_2/G was smaller than that of MnO_x/G-400, confirming Mn^{4+} played a predominate role in the composite (Fig. S2(c)) [54, 55]. The fitting peaks of O 1 s orbit of MnO_2/G is shown in Fig. S2(d) and the peak area percentage of Mn–O-H in MnO_2/G was higher than that in MnO_x/G-400 sample, illustrating some hydroxyl groups were removed after annealing [56]. In Fig. 6a, b, it can be observed that there appear some nanosheets in the TEM image of MnO_x/G-400, in accordance with the morphology in the SEM image. The high-resolution TEM image in Fig. 6c illustrates that MnO_x/G-400 consisted of both disorder region and different crystalline phases with several phase boundaries, further verifying the presence of the mixed phase junction. In Fig. 6d, the lattice fringes with the distance of 0.32 nm and 0.24 nm can be attributed to the (110) plane and (101) plane of α-MnO_2, which is in good agreement with the XRD pattern.

Figure 7 shows a radar chart summarizing and comparing five important characteristics of capacitive electrode materials, including areal capacitance, gravimetric capacitance, rate capability, capacitance retention and mass loading of the MnO_x/G-400 electrode and other reported Mn-based pseudocapacitive materials. At a current density of 1 mA cm^{-2}, the MnO_x/G-400 delivered a high areal capacitance of 2.29 F cm^{-2} and high gravimetric capacitance of 437 F g^{-1}. In addition, the electrode retained 97.4% capacitance after 5000 charge/discharge cycles, suggesting an excellent cyclic stability. The composite electrodes owned a mass loading of 5 ~ 8 mg cm^{-2} on carbon cloths without sacrificing electrochemical activities. Compared to other reported Mn-based composite electrodes, this mixed-valence metal oxide/rGO material exhibits the greater advantages and potential in improving capacitive performance.

Conclusion

In summary, a series of MnO_x/G composite electrodes was synthesized on flexible carbon cloths via a two-step hydrothermal route and annealing for improving capacitive properties. As the annealing temperature progressively increased, the product transforms from pure α-MnO_2/G into manganese oxide composites with lower valence state of Mn. The MnO_x/G-400 composite including Mn_2O_3 and α-

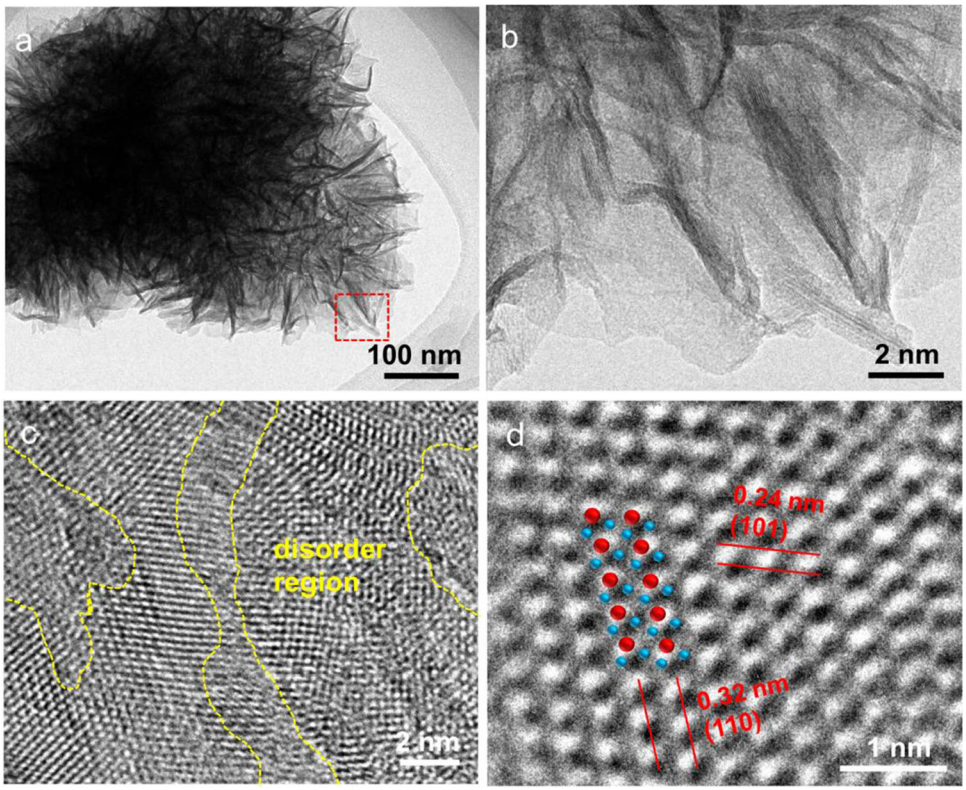

Figure 6 **a** TEM image of MnO_x/G-400. **b** Enlarged TEM image of Fig. 6(a). **c** Enlarged HRTEM image of MnO_x/G-400. **d** Enlarged HRTEM image of well-defined lattice fringe region of MnO_x/G-400.

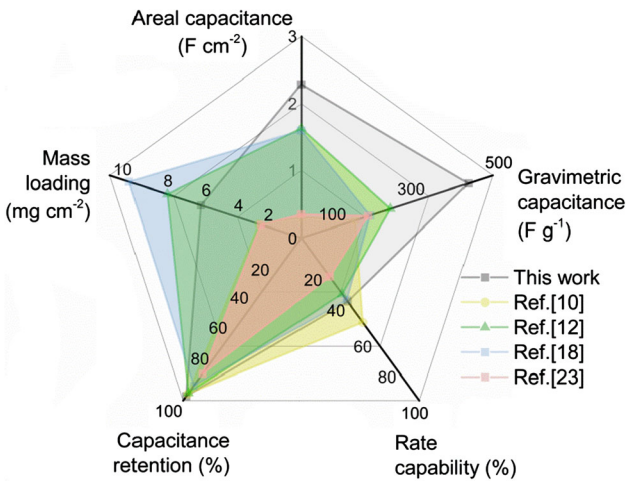

Figure 7 **a** Radar chart including gravimetric capacitance, areal capacitance, mass loading, rate capability (20-fold) and capacitance retention (after 5000 cycles) of the MnO_x/G-400 electrode and other reported pseudocapacitive materials (MnO_2/CC [10], $MnSiO_3$/C nanocomposite [12], MnO_x-h/CC [18], 3D graphene foam/CNT/MnO_2 [23]).

MnO_2 delivers the best electrochemical performance, due to the synergistic effect of the mixed phase. The MnO_x/G-400 electrode exhibits a high areal capacitance of 2.29 F cm^{-2} and a long lifespan owe to its mixed Mn(III)/(IV) phases and open 3D nanosheet structure. Besides, the reduced graphene oxide can not only contribute to total capacitance, but also promote the transfer of electron and ion between active materials and electrolyte, thereby facilitating fast Na^+ reaction kinetics. This work discloses a novel and scalable strategy to obtain high-performance capacitive materials based on metal oxide/-graphene composite via valence state regulation.

Acknowledgements

X.-X.L. thanks the support by the financial support from the National Natural Science Foundation of China (21673035). Y.S. acknowledges the financial support from the National Natural Science Foundation of China (51804066).

Declarations

Conflict of interest The authors declare that they have no conflicts of interest.

Supplementary Information: The online version contains supplementary material available at https://doi.org/10.1007/s10853-021-06613-7.

References

[1] Stoller MD, Ruoff RS (2010) Best practice methods for determining an electrode material's performance for ultracapacitors. Energy Environ Sci 3:1294–1301

[2] Gogotsi Y, Simon P (2011) True performance metrics in electrochemical energy storage. Science 334:917–918

[3] Zhao Y, Chen Z, Xiong DB, Qiao Y, Tang Y, Gao F (2016) Hybridized phosphate with ultrathin nanoslices and single crystal microplatelets for high performance supercapacitors. Sci Rep 6:17613–17622

[4] Wang G, Yang Y, Han D, Li Y (2017) Oxygen defective metal oxides for energy conversion and storage. Nano Today 13:23–39

[5] Peng X, Peng L, Wu C, Xie Y (2014) Two dimensional nanomaterials for flexible supercapacitors. Chem Soc Rev 43:3303–3323

[6] Wang W, Liu W, Zeng Y, Han Y, Yu M, Lu X, Tong Y (2015) A novel exfoliation strategy to significantly boost the energy storage capability of commercial carbon cloth. Adv Mater 27:3572–3578

[7] Yu M, Han Y, Cheng X, Hu L, Zeng Y, Chen M, Cheng F, Lu X, Tong Y (2015) Holey tungsten oxynitride nanowires: novel anodes efficiently integrate microbial chemical energy conversion and electrochemical Energy Storage. Adv Mater 27:3085–3091

[8] Xu C, Li Z, Yang C, Zou P, Xie B, Lin Z, Zhang Z, Li B, Kang F, Wong CP (2016) An ultralong, highly oriented nickel nanowire-array electrode scaffold for high-performance compressible pseudocapacitors. Adv Mater 28:4105–4110

[9] Yang J, Lian L, Ruan H, Xie F, Wei M (2014) Nanostructured porous MnO_2 on Ni foam substrate with a high mass loading via a CV electrodeposition route for supercapacitor application. Electrochim Acta 136:189–194

[10] Feng DY, Song Y, Huang ZH, Xu XX, Liu XX (2016) Rate capability improvement of polypyrrole via integration with functionalized commercial carbon cloth for pseudocapacitor. J Power Sources 324:788–797

[11] Lee JS, Shin DH, Jang J (2015) Polypyrrole-coated manganese dioxide with multiscale architectures for ultrahigh capacity energy storage. Energy Environ Sci 8:3030–3039

[12] Li B, Zhang X, Hu C, Dou J, Xia G, Zhang P, Zheng Z, Pan Y, Yu H, Chen C (2019) Mixed-valent $MnSiO_3$/C nanocomposite for high-performance asymmetric supercapacitor. J Colloid Interface Sci 556:239–248

[13] Lei Z, Zhang J, Zhao XS (2012) Ultrathin MnO_2 nanofibers grown on graphitic carbon spheres as high-performance asymmetric supercapacitor electrodes. J Mater Chem 22:153–160

[14] Toupin M, Brousse T, Bélanger D (2004) Charge storage mechanism of MnO_2 electrode used in aqueous electrochemical capacitor. Chem Mater 16:3184–3190

[15] Toupin M, Brousse T, Bélanger D (2002) Influence of microstucture on the charge storage properties of chemically synthesized manganese dioxide. Chem Mater 14:3946–3952

[16] Shi K, Pang X, Zhitomirsky I (2015) Fabrication of Tiron-doped polypyrrole/MWCNT composite electrodes with high mass loading and enhanced performance for supercapacitors. J Appl Polym Sci 132:42376–42376

[17] Xu P, Miao C, Cheng K, Ye K, Yin J, Cao D, Wang G, Zhang X (2016) Preparation of binder-free porous ultrathin $Ni(OH)_2$ nanoleafs using ZnO as pore forming agent displaying both high mass loading and excellent electrochemical energy storage performance. Electrochim Acta 216:499–509

[18] Song Y, Liu TY, Yao B, Li MY, Kou TY, Huang ZH, Feng DY, Wang FX, Tong YX, Liu XX, Li Y (2017) Ostwald ripening improves rate capability of high mass loading manganese oxide for supercapacitors. ACS Energy Lett 2:1752–1759

[19] Audi A, Sherwood P (2002) Valence-band X-ray photoelectron spectroscopic studies of manganese and its oxides interpreted by cluster and band structure calculations. Surf Interface Anal 33:274–282

[20] Zhu Y, Zhitomirsky I (2013) Influence of dopant structure and charge on supercapacitive behavior of polypyrrole electrodes with high mass loading. Synth Met 185–186:126–132

[21] Liu L, Weng W, Zhang J, Cheng X, Liu N, Yang J, Ding X (2016) Flexible supercapacitor with a record high areal specific capacitance based on a tuned porous fabric. J Mater Chem A 4:12981–12986

[22] Wang S, Zhu Z, Li P, Zhao C, Zhao C, Xia H (2018) In situ conversion of sub-4 nm $Co(OH)_2$ nanosheet arrays from phytic acid-derived $Co_3(HPO_4)_2(OH)_2$ for superior high loading supercapacitors. J Mater Chem A 6:20015–20024

[23] Liu JL, Zhang LL, Wu HB, Lin JY, Shen ZX, Lou XW (2014) High-performance flexible asymmetric supercapacitors based on a new graphene foam/carbon nanotube hybrid film. Energy Environ Sci 7:3709–3719

[24] Augustyn V, Simon P, Dunn B (2014) Pseudocapacitive oxide materials for high-rate electrochemical energy storage. Energy Environ Sci 7:1597–1614

[25] Lee JW, Hall AS, Kim JD, Mallouk TE (2012) A facile and template-free hydrothermal synthesis of Mn_3O_4 nanorods on graphene sheets for supercapacitor electrodes with long cycle stability. Chem Mater 24:1158–1164

[26] Chen Q, Lei S, Deng P, Ou X, Chen L, Wang W, Xiao Y, Cheng B (2017) Direct growth of nickel terephthalate on Ni

foam with large mass-loading for high-performance supercapacitors. J Mater Chem A 5:19323–19332

[27] Yang S, Wu C, Cai J, Zhu Y, Zhang H, Lu Y, Zhang K (2017) Seed-assisted smart construction of high mass loading Ni-Co-Mn hydroxide nanoflakes for supercapacitor applications. J Mater Chem A 5:16776–16785

[28] Ji HK, Lee YW, Jin HB (2013) Supercapacitor electrode with an ultrahigh Co_3O_4 loading for a high areal capacitance. Mater Lett 110:237–240

[29] Shen J, Li X, Wan L, Liang K, Tay BK, Kong L, Yan X (2017) An asymmetric supercapacitor with both ultra-high gravimetric and volumetric energy density based on 3D $Ni(OH)_2/MnO_2$@Carbon nanotube and activated polyaniline-derived Carbon. ACS Appl Mater Interfaces 9:668–676

[30] Tang Y, Liu Y, Guo W, Chen T, Wang H, Yu S, Gao F (2014) Highly oxidized graphene anchored $Ni(OH)_2$ nanoflakes as pseudocapacitor materials for ultrahigh loading electrode with high areal specific capacitance. J Phys Chem C 118:24866–24876

[31] Tao K, Li P, Kang L, Li X, Zhou Q, Dong L, Liang W (2015) Facile and low-cost combustion-synthesized amorphous mesoporous NiO/carbon as high mass-loading pseudocapacitor materials. J Power Sources 293:23–32

[32] Xin B, Zhao Y, Xu C (2016) A high mass loading electrode based on ultrathin Co_3S_4 nanosheets for high performance supercapacitor. J Solid State Electrochem 20:2197–2205

[33] Sarno M, Baldino L, Scudieri C, Cardea S, Ciambelli P, Reverchon E (2017) SC-CO_2-assisted process for a high energy density aerogel supercapacitor: the effect of GO loading. Nanotechnology 28:204001–204011

[34] Hu L, Chen W, Xie X, Liu N, Yang Y, Wu H, Yao Y, Pasta M, Alshareef HN, Cui Y (2011) Symmetrical MnO_2 carbon nanotube textile nanostructures for wearable pseudocapacitors with high mass loading. ACS Nano 5:8904–8913

[35] Wang S, Liu N, Rao J, Yue Y, Gao K, Su J, Li L, Jiang X, Liu Z, Gao Y (2017) Vertical finger-like asymmetric supercapacitors for enhanced performance at high mass loading and inner integrated photodetecting systems. J Mater Chem A 5:22199–22207

[36] Hu Z, Xiao X, Chen C, Li T, Huang L, Zhang C, Su J, Miao L, Jiang J, Zhang Y, Zhou J (2015) Al-doped α-MnO_2 for high mass-loading pseudocapacitor with excellent cycling stability. Nano Energy 11:226–234

[37] Pan Z, Liu M, Yang J, Qiu Y, Li W, Xu Y, Zhang X, Zhang Y (2017) High electroactive material loading on a carbon nanotube@3D graphene aerogel for high-performance flexible all-solid-state asymmetric supercapacitors. Adv Funct Mater 27:1701122–1701130

[38] Song Z, Li W, Bao Y, Sun Z, Gao L, Nawaz MH, Han D, Niu L (2018) Enhanced pseudocapacitance and electrolyte-wettability of graphene hydrogels to tailor high mass loading all-solid-state supercapacitor with ultra-high volumetric energy density. Carbon 136:46–53

[39] Hu Y, Guan C, Feng G, Ke Q, Huang X, Wang J (2016) Flexible asymmetric supercapacitor based on structure-optimized Mn_3O_4/reduced graphene oxide nanohybrid paper with high energy and power density. Adv Funct Mater 25:7291–7299

[40] He Y, Chen W, Li X, Zhang Z, Fu J, Zhao C, Xie E (2013) Freestanding three-dimensional graphene/MnO_2 composite networks as ultralight and flexible supercapacitor electrodes. ACS Nano 7:174–182

[41] Yan W, Ayvazian T, Kim J, Liu Y, Donavan K, Xing W, Yang Y, Hemminger J, Penner R (2011) Mesoporous manganese oxide nanowires for high-capacity, high-rate, hybrid electrical energy storage. ACS Nano 5:8275–8287

[42] Miao F, Shao C, Li X, Lu N, Wang K, Zhang X, Liu Y (2016) Polyaniline-coated electrospun carbon nanofibers with high mass loading and enhanced capacitive performance as freestanding electrodes for flexible solid-state supercapacitors. Energy 95:233–241

[43] Huang AX, Zhou WJ, Wang AR, Chen MF, Tian QH, Chen JZ (2021) Molten salt synthesis of α-MnO_2/Mn_2O_3 nanocomposite as a highperformance cathode material for aqueous zinc-ion batteries. J Energy Chem 54:475–481

[44] Wang SY, Cui YL, Cui B, Zhuang QC, Li B, Zheng H, Ju ZC (2019) δ-$MnO_2/KMnF_3$ composite with mixed valence as cathode for potassium ion battery. Adv Mater Interfaces 6:1901362. https://doi.org/10.1002/admi.201901362

[45] Chang L, Liu DQ, Zhou T, Hu M, Wang YC, Ge SM, He J, Li C, An CH (2020) The phase-change evolution from surface to bulk of MnO anodes upon cycling. Nanoscale 12:20425–20431

[46] Xiao Z, Ning G, Yu Z, Qi C, Zhao L, Li Y, Ma X, Li Y (2019) MnO@graphene nanopeapods derived *via* a one-pot hydrothermal process for a high performance anode in Li-ion batteries. Nanoscale 11:8270–8280

[47] Zhang L, Ge D, Qu G, Zheng J, Cao X, Gu H (2017) Formation of porous nitrogen-doped carbon-coating MnO nanospheres for advanced reversible lithium storage. Nanoscale. 9:5451–5457

[48] Wang T, Zhang QS, Zhong J, Chen MX, Deng HL, Cao JH, Wang L, Peng LL, Zhu J, Lu BA (2021) 3D holey graphene/polyacrylonitrile sulfur composite architecture for high loading lithium sulfur batteries. Adv Energy Mater 11:2100448. https://doi.org/10.1002/aenm.202100448

[49] Xu HJ, Wang L, Zhong J, Wang T, Cao J, Wang YY, Li X, Fei H, Zhu J, Duan XD (2020) Ultra-stable lithium-ion batteries based on MOF-derived In_2O_3 nanocrystals/

hierarchically porous nitrogen-doped carbon anode. Energy Environmental Materials 3:177–185

[50] Liu JL, Muhammad S, Wei ZX, Zhu J, Duan XF (2020) Hierarchical N-doping germanium/carbon nanofibers as anode for high-performance lithium-ion and sodium-ion batteries. Nanotechnology. 31:015402. https://doi.org/10.1088/1361-6528/ab4404

[51] Ning WW, Chen LB, Wei WF, Chen YJ, Zhang XY (2020) $NiCoO_2$/NiCoP@Ni nanowire arrays: tunable composition and unique structure design for high-performance winding asymmetric hybrid supercapacitors. Rare Met 39(9):1034–1044

[52] Li SY, He W, Liu B, Cui JQ, Wang XH, Peng DL, Liu B, Qu BH (2020) One-step construction of three-dimensional nickel sulfide-embedded carbon matrix for sodium-ion batteries and hybrid capacitors. Energy Storage Materials 25:636–643

[53] Wang YY, Zhao ZW, Liu Y, Hou LR, Yuan CZ (2020) Precipitant-free solvothermal construction of spindle-like $CoCO_3$/reduced graphene oxide hybrid anode toward high-performance lithium-ion batteries. Rare Met 39:1082–1091

[54] Ren Z, Wen J, Liu W, Jiang XP, Dong YH, Zhao QN, Ji GP, Wang RH, Hu N, Qu BH, Xu CH (2019) Rational design of layered SnS_2 on ultralight graphene fiber fabrics as binder-free anodes for enhanced practical capacity of sodium-ion batteries. Nano-Micro Lett 11:66. https://doi.org/10.1007/s40820-019-0297-6

[55] Sun F, Zhou D, He X, Osenberg M, Dong K, Chen LB, Mei SL, Hilger A, Markötter H, Lu Y, Dong S, Marathe S, Rau C, Hou X, Li J, Stan MC, Winter M, Dominko R, Manke I (2020) Morphological reversibility of modified Li-based anodes for next-generation batteries. ACS Energy Lett 5(1):152–161

[56] Wu C, Huang HF, Lu WY, Wei ZX, Ni XY, Sun F, Qing P, Liu Z, Ma JM, Wei WF, Chen LB, Yan CL, Mai LQ (2020) Mg doped Li–LiB alloy with in situ formed lithiophilic LiB skeleton for lithium metal batteries. Adv Sci 7:1902643. https://doi.org/10.1002/advs.201902643

Publisher's Note Springer Nature remains neutral with regard to jurisdictional claims in published maps and institutional affiliations.